scientific reports

Check for updates

OPEN

Utilizing photonic band gap in triangular silicon carbide structures for efficient quantum nanophotonic hardware

Pranta Saha✉, Sridhar Majety & Marina Radulaski

Silicon carbide is among the leading quantum information material platforms due to the long spin coherence and single-photon emitting properties of its color center defects. Applications of silicon carbide in quantum networking, computing, and sensing rely on the efficient collection of color center emission into a single optical mode. Recent hardware development in this platform has focused on angle-etching processes that preserve emitter properties and produce triangularly shaped devices. However, little is known about the light propagation in this geometry. We explore the formation of photonic band gap in structures with a triangular cross-section, which can be used as a guiding principle in developing efficient quantum nanophotonic hardware in silicon carbide. Furthermore, we propose applications in three areas: the TE-pass filter, the TM-pass filter, and the highly reflective photonic crystal mirror, which can be utilized for efficient collection and propagating mode selection of light emission.

Color centers are defects in wide band gap single-crystal materials that can emit single-photons and spin-entangled photons which act as quantum information carriers. Silicon carbide (SiC) is one of the most notable quantum hardware platforms since it hosts a collection of optically addressable color centers[1] with long spin coherence times[2–5], excellent brightness[6], nuclear spins[7,8], and telecommunication wavelength emissions[1,9], which are suitable properties for quantum information processing. On top of that, SiC has a large bandgap, high thermal conductivity, strong second-order nonlinearity, mechanical stability, and mature industrial presence[10,11] making it a reliable platform for a variety of applications. Recently, photonics in triangular geometry has come into focus for increasing the efficiency of such solid-state quantum emitter processes[5,9,12,13]. Triangular cross-section waveguide results from a bulk nanofabrication process called the angle-etch method that has been successfully implemented in both diamond[12,14] and SiC[5,13]. Previous fabrication processes were challenged by various imperfections that deteriorated the optical properties of the color centers or limited the robustness of the nanophotonic devices[9]. On the other hand, triangular geometry offers emitter implantation in bulk substrates (free-standing waveguides), which ensures high-quality color centers with better coupling and can pave the way for efficient quantum photonic hardware.

Advancement of quantum information technology greatly depends on the realization of robust quantum networks[9,15,16] and generation of arbitrary all-photonic cluster states[17–19] which, in color center platforms, are limited by the low photon collection efficiency. Color centers can have both transverse electric (TE) and transverse magnetic (TM) optical dipole-like emissions with a solid angle covering 4π. Hence, it is important to understand the TE/TM dispersion relations, in the triangular waveguide geometry, with a view to controlling and steering the quantum light emitted from the color center by PBG formation for higher collection efficiency.

The formation of photonic band gaps (PBGs) in photonic crystals (PhCs) has been explored in the past three decades after the discovery made by Yablonovitch and John[20,21]. Although wave propagation in periodic structures has almost been a century-long study[22], PhCs have gained attention due to their robust light confinement capability, scalability, and small footprint[23,24]. Combination of different scatterers with unique lattice geometries[10,11,25–33] has led to wider PBGs by reducing the structure symmetry and found applications in polarization beam splitters[34,35], optical logic gates[36,37], mirrors[38,39], sensors[40,41], lasers[42,43], solar cells[44,45], and more. Nevertheless, most of these studies have been conducted on either slab, rectangular, or cylindrical geometry. On the other hand, triangular cross-section PhCs have mostly been studied for constructing active photonic

Electrical and Computer Engineering Department, University of California, Davis, CA 95616, USA. ✉email: prsaha@ucdavis.edu

devices[13,46,47] whereas the dispersion relations and PBG formations are yet to be discussed in detail. We explore these properties to advance the photonic integration in SiC color center based quantum devices.

In this paper, we begin with defining the relevant parameters for analyzing PBG formation in SiC triangular cross-section PhCs. Using the plane wave expansion (PWE) method, we calculate the band structures and discuss the dispersion relations related to individual geometry. We then observe the effects of parameter variation on PBGs and examine the designs in terms of nanofabrication. We conclude by proposing three photonic devices along with their structural configurations and operational wavelength ranges which have the potential to be essential components of integrated photonic circuits.

Triangular cross-section photonic crystal

In this section, we define the parameters of the triangular cross-section photonic crystal. Traditionally, the periodic dielectric waveguides have periodicity along the direction of light propagation[48]. The triangular cross-section PhC in this study is realized in a similar fashion. Our 1D PhC structure is designed by inserting cylindrical air holes along y axis in the SiC triangular cross-section waveguide as shown in Figure 1a. The most significant parameters of the PhC are its lattice constant a, waveguide width w, hole radius r, and etch angle α. We examine three α values 35°, 45°, and 60°, which fall under realistic fabrication parameters of the state-of-the-art processes[5,13,49]. We vary the width w from $1.2a$ to $2.25a$, and the radius r from $0.25a$ to $0.45a$. We consider the refractive index of SiC to be $n_{\mathrm{SiC}} = 2.6$.

Based on the existence of a mirror symmetry plane ($z = 0$) perpendicular to the direction of periodicity, the photonic modes can be decoupled into TE-like and TM-like polarizations as illustrated in Fig. 1b. Modes with electric field lines having odd symmetry about $z = 0$ plane are TE-like as the main component of the electric field lies in the device plane. On the other hand, TM-like modes have even symmetry around $z = 0$ plane and the electric field lies in a direction perpendicular to the device plane.

We use the effective refractive index (n_{eff}) as a useful parameter for understanding the modal profiles in a photonic device[33,47,50]. It is defined as the ratio of propagation constant (β) of a mode to the vacuum wavenumber ($2\pi/\lambda$). In triangular geometry, the TE/TM polarized modes supported by the structure propagate according to their corresponding n_{eff} values. Modes with lower n_{eff} are not well contained within the structure and become evanescent[47]. As guided modes depend on n_{eff}, which is a strong function of the effective dielectric present in the photonic device, its value can help us interpret the dispersion relations and changes in PBGs due to parameter variation in the proposed 1D PhC. Hence, in the following, we come up with an analytical expression for estimated n_{eff} derived from the volumetric fill factor (VFF) of SiC in the PhC structure:

$$n_{\mathrm{eff}} = \mathrm{VFF} \times \mathrm{n_{SiC}} + (1 - \mathrm{VFF}) \times \mathrm{n_{air}} \tag{1}$$

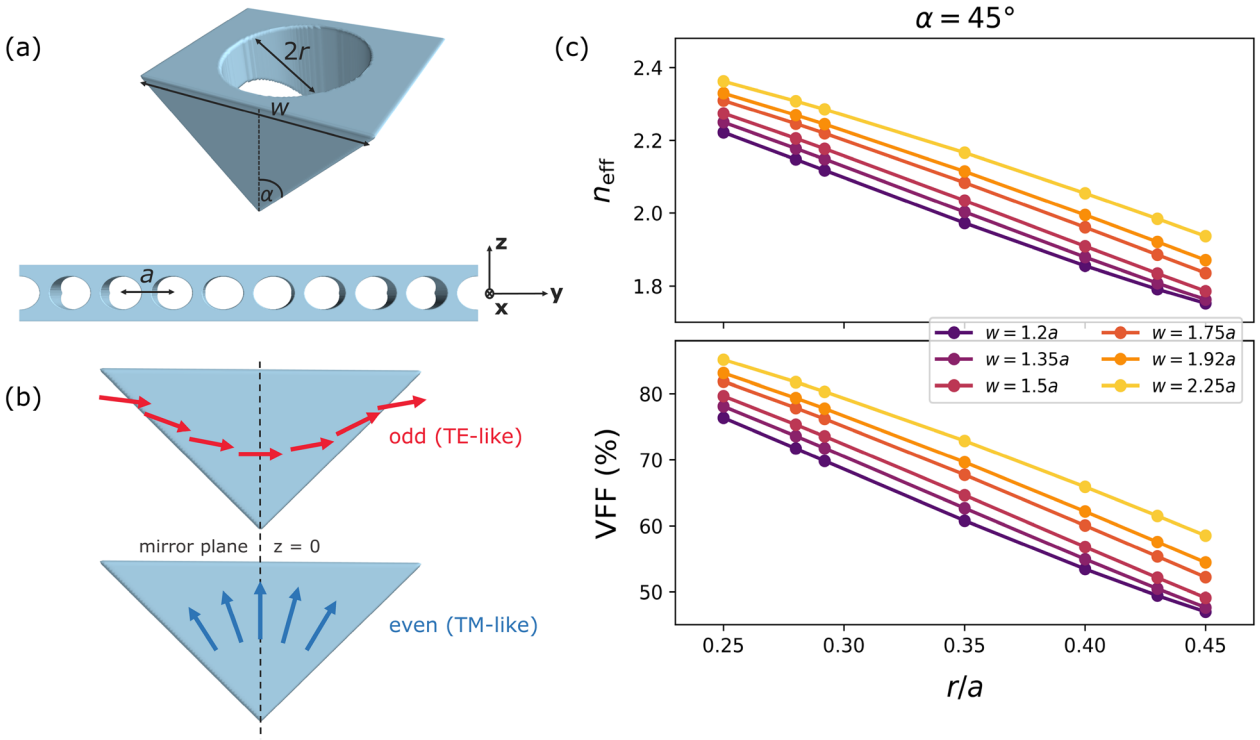

Figure 1. (**a**) Schematic of the 1D photonic crystal unit cell. (**b**) Electric field lines (arrow) associated with corresponding TE-like (red) and TM-like (blue) modes. (**c**) n_{eff} and VFF calculation as a function of r/a for $\alpha = 45°$.

Figure 1c demonstrates the changes in VFF and n_{eff} as a function of the normalized hole radii (r/a) in the 45° angle-etched waveguide with various w values. The plots show that n_{eff} reduces for higher r/a and increases for higher w. The latter happens due to the enlargement of the triangular cross-section with incremental w which leads to greater n_{eff} and more supported modes. We observe similar trends and values for 35° and 60°.

Methods

Dispersion relations in triangular geometry. While extensively studied in rectangular cross-section photonic crystals, the dispersion relations and PBG formations are not well understood in triangular geometry. Plane wave expansion (PWE) method has been widely used for analyzing PhCs due to its efficiency and accuracy in computing PBGs[31,51,52]. It is a direct frequency eigensolver method, derived from Maxwell's equations for a sourceless medium, where the eigenvalues are mode frequencies, and the eigenstates (plane wave solutions) are characterized by wavevector $\mathbf{k}$ and a band number. The irreducible Brillouin zone, which contains allowed wavevectors with non-redundant mode frequencies, lies in the range of (0, 0, 0) to $(0, \pi/a, 0)$ in the $\mathbf{k}$-space for 1D PhC according to our definition of periodicity[53]. We have used MIT Photonic Bands (MPB)[54] to employ the PWE method for investigating band structure and PBG formation in the above mentioned irreducible Brillouin zone of the triangular cross-section PhC.

The dispersion relations for three different PhC parameter sets (α, w, r) are presented in Fig. 2. In the band structure, the first TE/TM band (dielectric band) is the fundamental mode with the fewest nodes and the lowest frequency. The fundamental mode is well guided by the structure in all three PhCs. However, the higher-order mode (air band) for TE/TM is not entirely guided due to the light line effect, and becomes more radiative with α getting larger, as depicted in Fig. 2. The TE (red) and TM (blue) PBGs are formed between the minima of the air band and the maxima of the dielectric band of their respective polarizations. All three angle-etched 1D PhCs show both TE and TM band gaps. TE band gaps are larger than TM gaps due to the connected dielectric lattice structure which is in accordance with the general intuition[55]. Figure 2 also shows that 45° and 60° PhCs exhibit comparable TE gaps, while the TE band gap is reduced for 35° PhC. On the other hand, the TM gaps are comparable in 35° and 45° cases, and reduced for 60°.

Complete PBG refers to the region of forbidden propagation frequencies in the band structure regardless of polarization and is formed in the overlap of the TE and TM band gaps. Though conventional multilayered 1D PhCs lack a complete PBG[56], the triangular cross-section geometry offers complete PBG for all three studied angles α. As a number of color centers in SiC have both TE-like and TM-like emissions, it is desired to obtain a polarization-agnostic design with as wide complete PBG as possible. Figure 2 demonstrates that the largest complete PBG can be achieved with the 45° structure when the TM gap is completely buried within the TE gap. This condition occurs due to the TE gaps being larger than the TM gaps in our triangular cross-section photonic crystal design. Complete PBG in the other two cross-sections occurs from a small overlapping region between the TE and TM band gaps. Even though in two (w, r) sets, the 60° geometry shows buried complete PBGs, these gaps are about four times narrower compared to the 45° case. Therefore, 45° angle-etched triangular cross-section 1D PhC is more favorable for polarization-independent light confinement.

Effects of parameters on PBG formation for $\alpha = 45°$. In this section, we further analyze the effects of parameters to achieve the best performing design in the 45° angle-etched waveguide. Scale-invariant nature of Maxwell's equations actuates the idea of presenting parameters and results in terms of lattice constant a. Consequently, the gap width Δf, where f is frequency expressed in units of c/a, is not a useful measure to understand the extent of a PBG. The gap to midgap ratio $\Delta f/f_{\text{m}}$ (f_{m} is the midgap frequency), also known as the gap size, is a more telling characterization of the gap width as it is independent of the scaling. Figure 3 manifests TE-TM gap (c/a) and gap size (%) variation with r/a in $\alpha = 45°$ waveguides having several widths w. With incremental r/a, the n_{eff} decreases leading to an increase in f_{m} for both the TE and TM band gaps, consistent with the literature[57]. The opposite happens when w increases, due to the increased n_{eff}, for a corresponding r/a value.

In smaller w such as $1.2a$ and $1.35a$, the TE gap size initially increases with r/a owing to fewer supported modes as a result of lower VFF and n_{eff}, but shrinks after reaching the resonant condition at which the gap size is

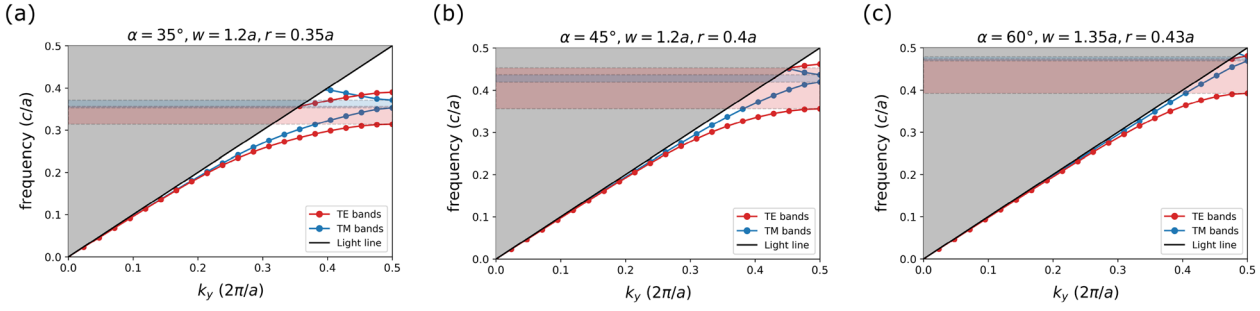

Figure 2. Dispersion relations for TE (red) and TM (blue) modes in the triangular cross-section 1D photonic crystal. The red (blue) shaded regions show the photonic band gaps for the TE (TM) modes. Parameters of the photonic crystal are: (**a**) $\alpha = 35°, w = 1.2a, r = 0.35a$. (**b**) $\alpha = 45°, w = 1.2a, r = 0.4a$. (**c**) $\alpha = 60°, w = 1.35a, r = 0.43a$.

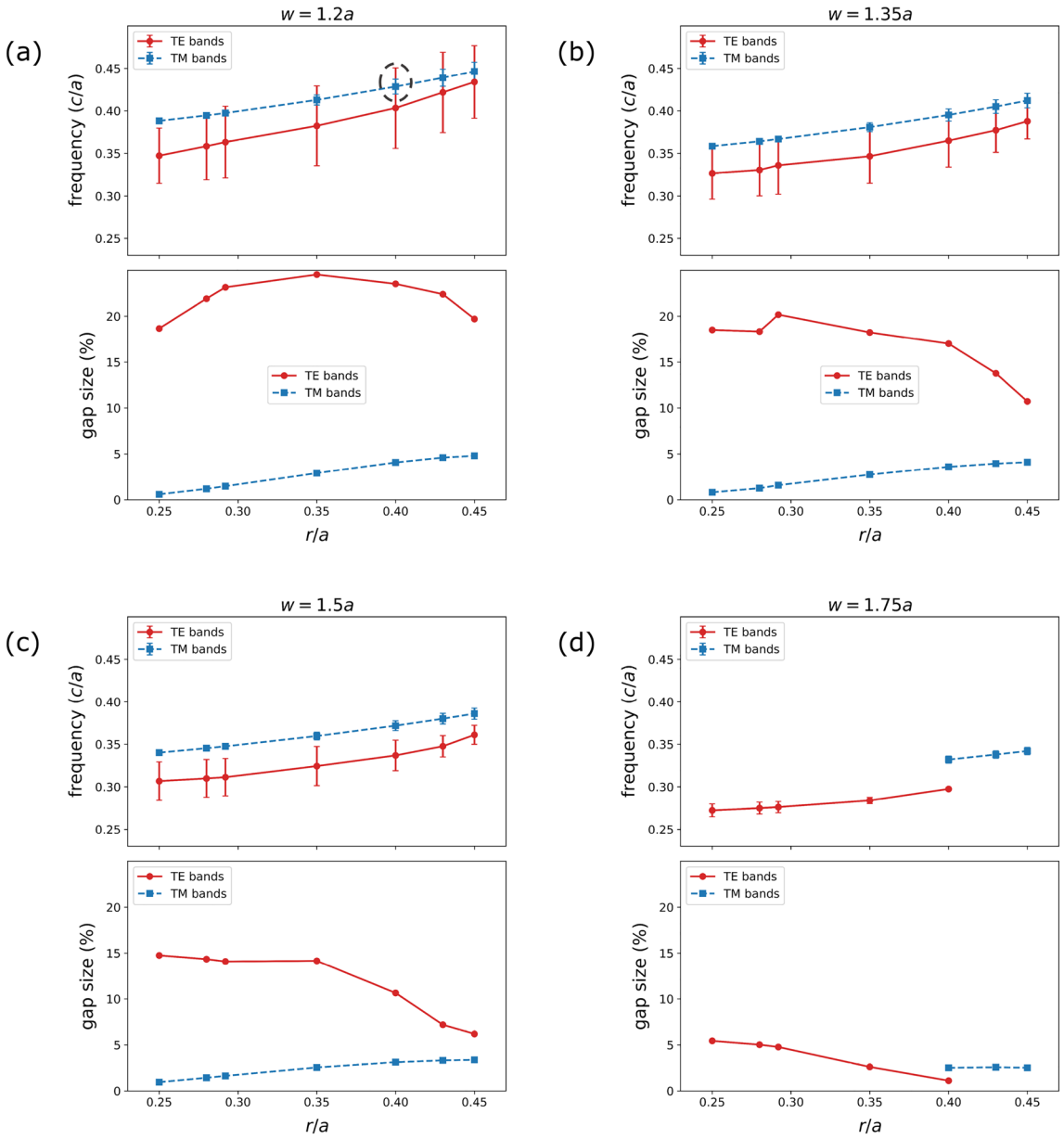

Figure 3. (**a**)–(**d**) TE/TM photonic band gap in frequency (c/a) and gap size (%) w.r.t. normalized hole radii (r/a) for the 45° triangular cross-section waveguide with w values of 1.2a, 1.35a, 1.5a, and 1.75a, respectively. In the frequency plots, the center points are midgap (f_m) frequencies and the error bars indicate band widths (Δf) for the corresponding TE/TM modes. The dashed circle shows the TE-TM gap overlap for the dispersion relations demonstrated in Fig. 2b.

maximum. This happens on account of the reduction in effective dielectric contrast with higher r/a values. Apparently, TE gap size in PhCs with larger widths w is smaller due to greater n_{eff}, and TE band gap vanishes above $w = 1.75a$. On the contrary, the TM gap size monotonically grows with r/a, however, the band gap disappears for larger widths, identical to the TE case. From Fig. 3 and the above discussion, it is evident that complete PBG (either buried or overlap) mostly occurs for smaller widths and TE/TM band gap totally vanishes for waveguides with larger widths ($w > 1.75a$).

Results and discussion

The demonstrated work provides insights into the dispersion relations in the non-standard, triangular, geometry of photonic crystals. Figure 4 delineates a general comparison of TE/TM gap sizes among three etch angles for a constant width ($w = 1.2a$). We observe that unique trend emerges from unique geometry. For the 35° triangular cross-section, the TE gap size appears stable with changes in hole radii, whereas the TM gap size variation is identical to the 45° case. On the other hand, the TE and TM gap sizes in the 60° geometry follow the same trend as the 45° TE case. In general, TE gaps in 35° and TM gaps in 60° cease to exist for PhCs with $w > 1.5a$.

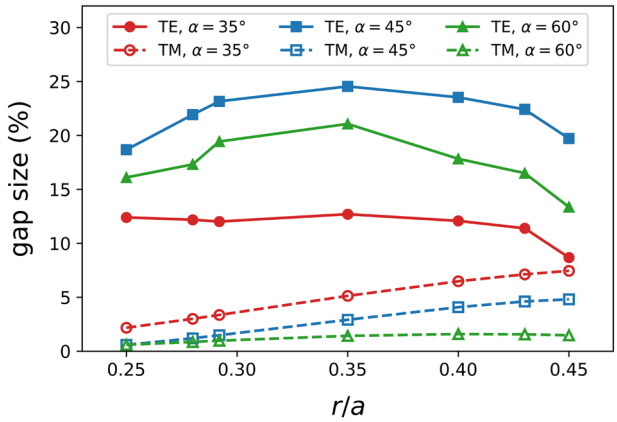

Figure 4. TE/TM gap size (%) in $w = 1.2a$ with varying normalized hole radii (r/a) for three α values.

In addition to discussing the formation of photonic band gaps in photonic crystals with variation in parameters, it is imperative to evaluate the practicality and robustness of the designs in terms of fabrication. For instance, it is challenging to fabricate larger holes ($r \geq 0.43a$) in smaller widths ($w \leq 1.35a$) because of the following two issues: i) there is $\leq$ 18% (of waveguide width w) space between the edge of the waveguide and the holes, and ii) only $\leq$ 14% (of unit cell a) room available between two adjacent holes. Therefore, a trade-off may need to be made deliberately, depending on the application, between the PBG size and the complexity of fabricating the device. Our recent work illustrates the design of a 60° angle-etched triangular cross-section 1D PhC mirror for enhancing the quantum efficiency of in situ superconducting nanowire single photon detectors (SNSPDs)[58]. Even though 60° geometry does not provide the largest complete PBG, waveguide in this geometry supports single mode propagation for NV center emission in 4H-SiC which is essential for single photon detection as well as quantum communication[59,60].

Individual geometry offers distinct applications based on the PBG formation. We foresee three such applications from which integrated photonics with triangular geometry can benefit greatly. Operational ranges, discussed in the following, are scaled to fit wavelengths of different 4H-SiC color center emissions by updating lattice constant a which depends on the choice of the center wavelength of the band gap.

Quantum communication through optical fiber network requires emission around the telecommunication bands for minimal loss of information. Vanadium (V^{4+}) defects in 4H-SiC covers the entire O-band spectrum with 25–50% Debye–Waller factor[61]. The photoluminescence features show that V^{4+} in 4H-SiC mostly emits TE-polarized light[62]. One can make a TE-pass filter (Figure 5a) for vanadium color center emission in the 1285–1344 nm range where the TM band gap forms in the 35° waveguide with $(a, w, r) = (390, 682, 156)$ nm photonic crystal parameters.

Silicon (V_{Si}) vacancy in 4H-SiC exhibits excellent optical stability and coherent spin control even in triangular waveguide structures with emissions from 861 nm to 918 nm[2,5,63]. The dipole polarization of single silicon vacancy center in 4H-SiC is mostly TM[64] and 60° waveguide with $(a, w, r) = (337, 590, 135)$ nm operates as a TM-pass filter (Fig. 5c) for V_{Si} emission from 840 nm to 1015 nm where the TE band gap is formed.

Longer spin coherence time is necessary for photonic-cluster based quantum computation and communication. With the combination of isotopic purification and dynamic decoupling, spin coherence time of 5s has been reported in neutral divacancy (VV^0) in SiC[65] which is the highest among the defect spin qubits in SiC. Due to the nature of electronic structure, selection rules, and symmetry[66,67], divacancy emission has both TE and TM polarizations with zero-phonon line ranging from 1078 to 1132 nm. A polarization-independent mirror (Fig. 5b) for divacancy emission can be constructed using the 45° waveguide with the parameters $(a, w, r) = (475, 570, 190)$ nm that provides complete PBG from 1087 nm to 1132 nm. This happens because of the large overlapping TE-TM band gap region formed in the $\alpha = 45°$ triangular cross-section waveguide PhC.

Conclusion

Photonic integration of SiC color centers is known to enhance the efficiency of quantum hardware[16]. Here, the triangular geometry of devices can provide a combination of the pristine optical properties of the implanted color centers and the sample-agnostic nanofabrication. We have presented how photonic band gaps can be formed and applied in this geometry. As color centers have optical dipole-like emissions, the exploration of the dispersion relations and PBG formations in triangular cross-section 1D PhCs can play a significant role for robust light confinement in quantum photonic hardware. Our simulated results show that the nature of PBG configurations primarily depends on the etch-angle and varies intuitively with other PhC parameters. The three proposed devices can control quantum light propagation with mode selectivity and the parameter features are suitable for nanofabrication as well. These designs have the potential to improve the performance of integrated photonic devices with applications in quantum communication and quantum computing.

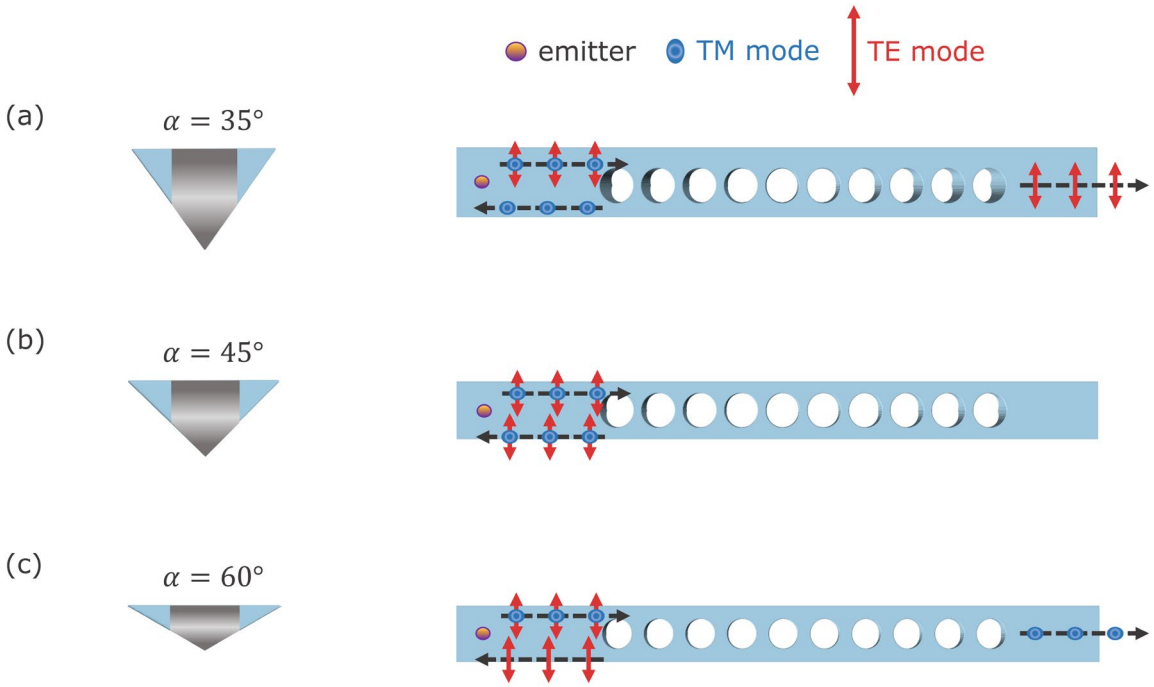

Figure 5. (**a**) TE-pass filter in 35° waveguide with $(a, w, r) = (390, 682, 156)$ nm. (**b**) Polarization-independent mirror in 45° waveguide with $(a, w, r) = (475, 570, 190)$ nm. (**c**) TM-pass filter in 60° waveguide with $(a, w, r) = (337, 590, 135)$ nm. The dashed (black) arrow shows the direction of light propagation.

Data availability

The data that support the findings of this study are available upon reasonable request from the corresponding author Pranta Saha (prsaha@ucdavis.edu).

Received: 23 December 2022; Accepted: 10 March 2023
Published online: 13 March 2023

References

1. Norman, V. A. *et al.* Novel color center platforms enabling fundamental scientific discovery. *InfoMat* **3**, 869–890 (2021).
2. Widmann, M. *et al.* Coherent control of single spins in silicon carbide at room temperature. *Nat. Mater.* **14**, 164–168 (2015).
3. Christle, D. J. *et al.* Isolated electron spins in silicon carbide with millisecond coherence times. *Nat. Mater.* **14**, 160–163 (2015).
4. Seo, H. *et al.* Quantum decoherence dynamics of divacancy spins in silicon carbide. *Nat. Commun.* **7**, 1–9 (2016).
5. Babin, C. *et al.* Fabrication and nanophotonic waveguide integration of silicon carbide colour centres with preserved spin-optical coherence. *Nat. Mater.* **21**, 67–73 (2022).
6. Castelletto, S. *et al.* A silicon carbide room-temperature single-photon source. *Nat. Mater.* **13**, 151–156 (2014).
7. Falk, A. L. *et al.* Optical polarization of nuclear spins in silicon carbide. *Phys. Rev. Lett.* **114**, 247603 (2015).
8. Klimov, P. V., Falk, A. L., Christle, D. J., Dobrovitski, V. V. & Awschalom, D. D. Quantum entanglement at ambient conditions in a macroscopic solid-state spin ensemble. *Sci. Adv.* **1**, e1501015 (2015).
9. Majety, S., Saha, P., Norman, V. A. & Radulaski, M. Quantum information processing with integrated silicon carbide photonics. *J. Appl. Phys.* **131**, 130901 (2022).
10. Song, B.-S., Yamada, S., Asano, T. & Noda, S. Demonstration of two-dimensional photonic crystals based on silicon carbide. *Opt. Express* **19**, 11084–11089 (2011).
11. Radulaski, M. *et al.* Photonic crystal cavities in cubic (3C) polytype silicon carbide films. *Opt. Express* **21**, 32623–32629 (2013).
12. Burek, M. J. *et al.* Free-standing mechanical and photonic nanostructures in single-crystal diamond. *Nano Lett.* **12**, 6084–6089 (2012).
13. Song, B.-S. *et al.* High-Q-factor nanobeam photonic crystal cavities in bulk silicon carbide. *Appl. Phys. Lett.* **113**, 231106 (2018).
14. Atikian, H. A. *et al.* Freestanding nanostructures via reactive ion beam angled etching. *APL Photon.* **2**, 051301 (2017).
15. Ruf, M., Wan, N. H., Choi, H., Englund, D. & Hanson, R. Quantum networks based on color centers in diamond. *J. Appl. Phys.* **130**, 070901 (2021).
16. Castelletto, S. *et al.* Silicon carbide photonics bridging quantum technology. *ACS Photon.* **9**, 1434–1457 (2022).
17. Lindner, N. H. & Rudolph, T. Proposal for pulsed on-demand sources of photonic cluster state strings. *Phys. Rev. Lett.* **103**, 113602 (2009).
18. Buterakos, D., Barnes, E. & Economou, S. E. Deterministic generation of all-photonic quantum repeaters from solid-state emitters. *Phys. Rev. X* **7**, 041023 (2017).
19. Russo, A., Barnes, E. & Economou, S. E. Generation of arbitrary all-photonic graph states from quantum emitters. *New J. Phys.* **21**, 055002 (2019).
20. Yablonovitch, E. Inhibited spontaneous emission in solid-state physics and electronics. *Phys. Rev. Lett.* **58**, 2059 (1987).
21. John, S. Strong localization of photons in certain disordered dielectric superlattices. *Phys. Rev. Lett.* **58**, 2486 (1987).
22. Born, M. Wave propagation in periodic structures. *Nature* **158**, 926–926 (1946).
23. Shakoor, A. *et al.* Compact 1D-silicon photonic crystal electro-optic modulator operating with ultra-low switching voltage and energy. *Opt. Express* **22**, 28623–28634 (2014).

24. Zhou, T. *et al.* Single-mode photonic crystal nanobeam lasers monolithically grown on Si for dense integration. *IEEE J. Sel. Top. Quantum Electron.* **28**, 1–6 (2021).
25. Villeneuve, P. R. & Piché, M. Photonic band gaps in two-dimensional square lattices: Square and circular rods. *Phys. Rev. B* **46**, 4973 (1992).
26. Wang, R., Wang, X.-H., Gu, B.-Y. & Yang, G.-Z. Effects of shapes and orientations of scatterers and lattice symmetries on the photonic band gap in two-dimensional photonic crystals. *J. Appl. Phys.* **90**, 4307–4313 (2001).
27. Johnson, S. G., Povinelli, M. L. & Joannopoulos, J. D. New photonic crystal system for integrated optics. In *Active and Passive Optical Components for WDM Communication*, Vol. 4532, 167–179 (SPIE, 2001).
28. Notomi, M., Kuramochi, E. & Taniyama, H. Ultrahigh-Q nanocavity with 1D photonic gap. *Opt. Express* **16**, 11095–11102 (2008).
29. Kalra, Y. & Sinha, R. Modelling and design of complete photonic band gaps in two-dimensional photonic crystals. *Pramana* **70**, 153–161 (2008).
30. Zhou, J. *et al.* Facile fabrication of tough SiC inverse opal photonic crystals. *J. Phys. Chem. C* **114**, 22303–22308 (2010).
31. Quan, Q. & Loncar, M. Deterministic design of wavelength scale, ultra-high Q photonic crystal nanobeam cavities. *Opt. Express* **19**, 18529–18542 (2011).
32. Eguchi, M. & Tsuji, Y. Single-polarization elliptical-hole lattice core photonic-bandgap fiber. *J. Lightwave Technol.* **31**, 177–182 (2012).
33. Shi, J. *et al.* Photonic crystal and quasi-crystals providing simultaneous light coupling and beam splitting within a low refractive-index slab waveguide. *Sci. Rep.* **7**, 1–10 (2017).
34. Hou, J., Wang, L., Yang, C., Wang, B. & Chen, S. Compact high extinction ratio asymmetric polarization beam splitter of periodic rods waveguide. *Appl. Opt.* **54**, 10277–10282 (2015).
35. Butt, M. & Kazanskiy, N. Two-dimensional photonic crystal heterostructure for light steering and TM-polarization maintaining applications. *Laser Phys.* **31**, 036201 (2021).
36. Anagha, E. & Jeyachitra, R. An investigation on the cascaded operation of photonic crystal based all optical logic gates and verification of de morgan's law. *Opt. Quant. Electron.* **52**, 1–26 (2020).
37. Swarnakar, S., Rathi, S. & Kumar, S. Design of all optical XOR gate based on photonic crystal ring resonator. *J. Opt. Commun.* **41**, 51–56 (2020).
38. Zhao, D., Yang, H., Ma, Z. & Zhou, W. Polarization independent broadband reflectors based on cross-stacked gratings. *Opt. Express* **19**, 9050–9055 (2011).
39. Zhong, Y. K., Fu, S. M., Yan, S. L., Chen, P. Y. & Lin, A. Arbitrarily-wide-band dielectric mirrors and their applications to SiGe solar cells. *IEEE Photon. J.* **7**, 1–12 (2015).
40. Scullion, M., Di Falco, A. & Krauss, T. Slotted photonic crystal cavities with integrated microfluidics for biosensing applications. *Biosens. Bioelectron.* **27**, 101–105 (2011).
41. Zhuo, Y. *et al.* Single nanoparticle detection using photonic crystal enhanced microscopy. *Analyst* **139**, 1007–1015 (2014).
42. Painter, O. *et al.* Two-dimensional photonic band-gap defect mode laser. *Science* **284**, 1819–1821 (1999).
43. Lu, H.-Y. *et al.* Extracting more light for vertical emission: high power continuous wave operation of 1.3-μm quantum-dot photonic-crystal surface-emitting laser based on a flat band. *Light Sci. Appl.* **8**, 1–6 (2019).
44. Bermel, P., Luo, C., Zeng, L., Kimerling, L. C. & Joannopoulos, J. D. Improving thin-film crystalline silicon solar cell efficiencies with photonic crystals. *Opt. Express* **15**, 16986–17000 (2007).
45. Hwang, D.-K., Lee, B. & Kim, D.-H. Efficiency enhancement in solid dye-sensitized solar cell by three-dimensional photonic crystal. *RSC Adv.* **3**, 3017–3023 (2013).
46. Burek, M. J. *et al.* High quality-factor optical nanocavities in bulk single-crystal diamond. *Nat. Commun.* **5**, 1–7 (2014).
47. Majety, S. *et al.* Quantum photonics in triangular-cross-section nanodevices in silicon carbide. *J. Phys. Photon.* **3**, 034008 (2021).
48. Fan, S. *et al.* Guided and defect modes in periodic dielectric waveguides. *JOSA B* **12**, 1267–1272 (1995).
49. Cranwell Schaeper, O. *et al.* Fabrication of photonic resonators in bulk 4H-SiC. *Adv. Mater. Technol.* **6**, 2100589 (2021).
50. Chen, G. *et al.* Wavelength selective mode division multiplexing on a silicon chip. *Opt. Express* **23**, 8095–8103 (2015).
51. Shi, S., Chen, C. & Prather, D. W. Plane-wave expansion method for calculating band structure of photonic crystal slabs with perfectly matched layers. *JOSA A* **21**, 1769–1775 (2004).
52. Panda, A. & Pukhrambam, P. D. Analysis of GaN-based 2D photonic crystal sensor for real-time detection of alcohols. *Braz. J. Phys.* **51**, 481–492 (2021).
53. Joannopoulos, J. D., Johnson, S. G., Winn, J. N. & Meade, R. D. *Photonic Crystals: Molding the Flow of Light* 2nd edn. (Princeton University Press, Princeton, 2008).
54. Johnson, S. G. & Joannopoulos, J. D. Block-iterative frequency-domain methods for Maxwell's equations in a planewave basis. *Opt. Express* **8**, 173–190 (2001).
55. Joannopoulos, J. D., Villeneuve, P. R. & Fan, S. Photonic crystals: Putting a new twist on light. *Nature* **386**, 143–149 (1997).
56. Butt, M., Khonina, S. & Kazanskiy, N. Recent advances in photonic crystal optical devices: A review. *Opt. Laser Technol.* **142**, 107265 (2021).
57. Anderson, P. D. & Subramania, G. Unidirectional edge states in topological honeycomb-lattice membrane photonic crystals. *Opt. Express* **25**, 23293–23301 (2017).
58. Majety, S. *et al.* Triangular quantum photonic devices with integrated detectors in silicon carbide. arXiv preprint arXiv:2208.05569 (2022).
59. Yusof, R., Ali, N., Kolenderski, P., Slowik, K. & Hambali, N. A. Comparative studies of rib waveguide material for quantum communication application. In *IOP Conference Series: Materials Science and Engineering*, Vol. 551, 012018 (2019).
60. Westig, M., Thierschmann, H., Katan, A., Finkel, M. & Klapwijk, T. M. Analysis of a single-mode waveguide at sub-terahertz frequencies as a communication channel. *AIP Adv.* **10**, 015008 (2020).
61. Wolfowicz, G. *et al.* Vanadium spin qubits as telecom quantum emitters in silicon carbide. *Sci. Adv.* **6**, eaaz1192 (2020).
62. Spindlberger, L. *et al.* Optical properties of vanadium in 4h silicon carbide for quantum technology. *Phys. Rev. Appl.* **12**, 014015 (2019).
63. Nagy, R. *et al.* High-fidelity spin and optical control of single silicon-vacancy centres in silicon carbide. *Nat. Commun.* **10**, 1–8 (2019).
64. Radulaski, M. *et al.* Scalable quantum photonics with single color centers in silicon carbide. *Nano Lett.* **17**, 1782–1786 (2017).
65. Anderson, C. P. *et al.* Five-second coherence of a single spin with single-shot readout in silicon carbide. *Sci. Adv.* **8**, eabm5912 (2022).
66. Economou, S. E. & Dev, P. Spin-photon entanglement interfaces in silicon carbide defect centers. *Nanotechnology* **27**, 504001 (2016).
67. Wang, J.-F. *et al.* Experimental optical properties of single nitrogen vacancy centers in silicon carbide at room temperature. *ACS Photon.* **7**, 1611–1616 (2020).

Acknowledgements

This work is supported by the National Science Foundation (CAREER-2047564).

Author contributions

P.S. performed the simulations, P.S. and S.M. analyzed the data, M.R. supervised the project. All authors contributed to the manuscript writing.

Competing interests

The authors declare no competing interests.

Additional information

Correspondence and requests for materials should be addressed to P.S.

Reprints and permissions information is available at www.nature.com/reprints.

Publisher's note Springer Nature remains neutral with regard to jurisdictional claims in published maps and institutional affiliations.